

# **JGR** Planets

## RESEARCH ARTICLE

10.1029/2025JE009244

#### **Key Points:**

- Curiosity encountered dark-toned veins while traversing the Chenapau member in the sulfate-bearing unit of Gale crater's central mound
- Mastcam and ChemCam observations indicate that these veins are composed of a mixture of halite and host rock material
- These veins are compositionally distinct from veins found previously in the mission and record a transition to a drier, saline environment

#### **Supporting Information:**

Supporting Information may be found in the online version of this article.

#### Correspondence to:

A. R. Trussell, atrussell@asu.edu

#### Citation:

Trussell, A. R., Bell, J. F., III, Farrand, W. H., Hughes, E. B., Eng, A. M., Kah, L. C., et al. (2025). Dark-toned halite-enriched veins above the Marker Band record a drying environment in Gale crater. *Journal of Geophysical Research: Planets*, 130, e2025JE009244. https://doi.org/10.1029/2025JE009244

Received 12 JUN 2025 Accepted 6 OCT 2025

## **Author Contributions:**

Conceptualization: A. R. Trussell Data curation: A. R. Trussell, E. B. Hughes, A. M. Eng, C. D. O'Connell-Cooper, L. M. Thompson, H. T. Manelski, R. Y. Sheppard, B. S. Douglass, G. Paar, S. Le Mouélic

Formal analysis: A. R. Trussell, L. C. Kah Funding acquisition: A. R. Trussell, J. F. Bell III

Investigation: A. R. Trussell, J. F. Bell III, W. H. Farrand, L. C. Kah, C. D. O'Connell-Cooper, P. J. Gasda,

H. T. Manelski, S. G. Banham, C. A. Mondro, J. R. Johnson, G. Paar, F. Gómez

## © 2025 The Author(s).

This is an open access article under the terms of the Creative Commons Attribution-NonCommercial License, which permits use, distribution and reproduction in any medium, provided the original work is properly cited and is not used for commercial purposes.

# Dark-Toned Halite-Enriched Veins Above the Marker Band Record a Drying Environment in Gale Crater

A. R. Trussell<sup>1</sup> , J. F. Bell III<sup>1</sup>, W. H. Farrand<sup>2</sup> , E. B. Hughes<sup>3</sup> , A. M. Eng<sup>3</sup> , L. C. Kah<sup>4</sup> , C. D. O'Connell-Cooper<sup>5</sup> , L. M. Thompson<sup>5</sup> , P. J. Gasda<sup>6</sup> , H. T. Manelski<sup>7</sup> , R. Y. Sheppard<sup>8,9</sup> , S. G. Banham<sup>10</sup> , C. A. Mondro<sup>11</sup> , B. S. Douglass<sup>1</sup>, J. R. Johnson<sup>12</sup> , G. Paar<sup>13</sup> , O. Gasnault<sup>14</sup> , A. R. Vasvada<sup>15</sup> , F. Gómez<sup>16</sup> , S. Le Mouélic<sup>17</sup> , O. Forni<sup>14</sup> , and P.-Y. Meslin<sup>14</sup>

<sup>1</sup>Arizona State University, Tempe, AZ, USA, <sup>2</sup>Space Science Institute, Boulder, CO, USA, <sup>3</sup>Georgia Institute of Technology, Atlanta, GA, USA, <sup>4</sup>University of Tennessee, Knoxville, TN, USA, <sup>5</sup>University of New Brunswick, Fredericton, NB, Canada, <sup>6</sup>Los Alamos National Laboratory, Los Alamos, NM, USA, <sup>7</sup>Purdue University, West Lafayette, IN, USA, <sup>8</sup>Planetary Science Institute, Tucson, AZ, USA, <sup>9</sup>Institut d'Astrophysique Spatiale, Orsay, France, <sup>10</sup>Imperial College, London, UK, <sup>11</sup>California Institute of Technology, Pasadena, CA, USA, <sup>12</sup>Johns Hopkins University Applied Physics Laboratory, Laurel, MD, USA, <sup>13</sup>Joanneum Research, Graz, Austria, <sup>14</sup>Institut de Recherche en Astrophysique et Planétologie (IRAP), Université Paul Sabatier, Toulouse, France, <sup>15</sup>Jet Propulsion Laboratory, California Institute of Technology, Pasadena, CA, USA, <sup>16</sup>Centro de Astrobiología (INTA-CSIC), Madrid, Spain, <sup>17</sup>Laboratoire de Planétologie et Géosciences, UMR 6112, Nantes Université, Nantes, France

**Abstract** The Martian surface preserves evidence of a global climate transition from wetter to drier conditions, but the nature of the fluids involved in this evolution remains poorly constrained. In Gale crater, the clay-sulfate transition and presence of evaporite mineral assemblages can provide insights into the properties of these fluids and the timing of environmental change. While traversing through the Chenapau member of the sulfate-bearing unit in Gale crater, the Curiosity rover encountered a set of dark-toned veins enriched in Na and Cl, suggestive of halite. However, previous halite detections in Gale crater have been limited to occurrences along the edges of Ca-sulfate veins or nodules, suggesting a unique origin for this set of veins. Here, we hypothesize that these veins formed through the infiltration of saline fluids along pre-existing hydraulically induced fractures. These fluids permeated into the host rock beyond the primary fractures, precipitating halite and cementing the fractures. Using Mastcam and ChemCam spectra, we found that the veins displayed a downturn in the near-infrared wavelengths, consistent with the presence of ferrous iron. Furthermore, textural analysis of the veins reveals host rock material preserved within the veins. ChemCam laser-induced breakdown spectroscopy observations also support the presence of a minor Fe component in the veins and halite concentrated along the center of the fractures. Our results demonstrate that these veins represent a distinct class of diagenetic features in Curiosity's mission that record an important transition in near-surface fluid chemistry consistent with a transition to a drier environment.

Plain Language Summary Mars experienced a major climate transition from wet to dry, and this transition is recorded in the geologic units in Gale crater that are being explored by the Curiosity rover. Data from Curiosity reveal dark-toned, Na- and Cl-rich deposits filling fractures within the rocks (veins), indicating the presence of halite (salt) in the sulfate-bearing unit. This finding is notable because previous halite detections in Gale crater have been isolated to individual grains or along the boundaries of pre-existing veins, suggesting a different formation process for the veins described here. We investigated images and data from Curiosity's instruments to characterize the chemical composition and formation of these veins. We found that these veins likely formed when sedimentary layers were buried in Gale crater, leading to a large overburden pressure and the over pressurization of the fluids trapped in these rocks. The over pressurized fluids then caused the rocks to fracture. Later, saline fluids flowed along the fractures and a small degree beyond the fracture into the surrounding host rock, depositing halite. These findings record a change in fluid chemistry that supports a transition from a wetter to a drier environment, and that fluid stability continued even in the drier sulfate-bearing unit.

#### 1. Introduction

The geologic record of Mars preserves a story of climate change, as evidenced by changes in mineralogy, ancient outflow channels, layered sedimentary deposits, and loss of water to space (e.g., Bishop & Rampe, 2016;

TRUSSELL ET AL. 1 of 17



10.1029/2025JE009244

Methodology: A. R. Trussell, W. H. Farrand, H. T. Manelski, R. Y. Sheppard, B. S. Douglass Resources: J. F. Bell III, G. Paar, S. Le Software: E. B. Hughes, A. M. Eng Supervision: J. F. Bell III Visualization: A. R. Trussell, H. T. Manelski, G. Paar Writing - original draft: A. R. Trussell, Writing - review & editing: A. R. Trussell, J. F. Bell III, W. H. Farrand, E. B. Hughes, A. M. Eng, C. D. O'Connell-Cooper, L. M. Thompson, P. J. Gasda, H. T. Manelski, S. G. Banham, C. A. Mondro, J. R. Johnson, G. Paar, O. Gasnault, A. R. Vasvada, F. Gómez,

S. Le Mouélic, O. Forni, P.-Y. Meslin

Jakosky, 2021; Malin & Edgett, 2000; Rodriguez et al., 2015; Scheller et al., 2021). One of the reasons Gale crater was selected as the landing site for the Mars Science Laboratory (MSL) Curiosity rover was because of the upward transition from phyllosilicate-enriched to sulfate-enriched strata observed in orbital data of the crater's central sedimentary mound, Aeolis Mons (informally Mount Sharp) (e.g., Milliken et al., 2010; Thomson et al., 2011). This transition suggests a shift from an ancient wetter environment to a drier one (Bibring et al., 2006; Grotzinger et al., 2012; Milliken et al., 2010). Curiosity found mudstones in Yellowknife Bay that likely formed in a neutral pH, shallow lacustrine environment capable of supporting life (Grotzinger et al., 2014). As Curiosity has ascended the lower flank of Mount Sharp, the rover has found evidence for a drying environment as indicated by, for example, the presence of desiccation cracks and polygonal ridges (Rapin et al., 2023; Stein et al., 2018), dehydration of Ca-sulfate veins (Rapin et al., 2016), the transition from clays to crystalline Mg-sulfates (Chipera et al., 2023), and the presence of aeolian scours (Roberts et al., 2025). However, the exact nature and timing of this transition remain unclear, including whether the transition was abrupt or involved a longer period of wet-dry cycling.

Veins can provide geochemical constraints to this transition because of their ability to record the chemistry of post-depositional fluids that have altered rocks. The types of fractures that vein minerals fill also provide information about the stresses that have affected the rock post-emplacement. Throughout the mission, Curiosity has encountered diverse diagenetic features such as veins (Banham et al., 2025; De Toffoli et al., 2020; Kronyak et al., 2019; L'Haridon et al., 2018; Nachon et al., 2014; Rapin et al., 2016), nodules (Gasda et al., 2022; Meyer et al., 2024; Stack et al., 2014; Treiman et al., 2023; VanBommel et al., 2023), concretions (Banham et al., 2018; Seeger & Grotzinger, 2024; Wiens et al., 2017), ridges (Banham et al., 2024; Léveillé et al., 2014; McLennan et al., 2014), and dendritic aggregates (Nachon et al., 2017) that reveal distinct episodes of fluid interaction with rocks

In 2023, Curiosity encountered dark-toned fracture-filling material while traversing the Chenapau member of the Mirador formation above the Marker Band Valley (Figure 1) (e.g., Roberts et al., 2024). Elemental chemistry from Curiosity's ChemCam instrument showed that these fracture-fills are enriched in Na and Cl, suggestive of halite (Farrand et al., 2023; Meslin et al., 2024). Prior to entering the sulfate unit, detection of halite was limited to isolated grains in bedrock or along the edges of Ca-sulfate veins (Meslin et al., 2022, 2024; Thomas et al., 2019). These Na- and Cl-enriched fracture fills could represent a distinct episode of fluid flow, characterized by more arid conditions that allowed for the precipitation of contiguous halite (Meslin et al., 2024). Here, we investigate the composition, texture, and morphology of these veins in more detail through a combination of Mastcam and ChemCam data to understand their formation mechanism and relation to the surrounding bedrock.

### 2. Background

## 2.1. Geologic Context

Curiosity has been exploring the Gale crater, a  $\sim$ 155 km diameter impact crater situated along the dichotomy boundary (Milliken et al., 2010). The rover has been ascending Mount Sharp (Aeolis Mons), a 5.5 km thick sequence of sedimentary deposits inside Gale crater. Mount Sharp is the eroded remnant of the sedimentary infilling of Gale (Malin & Edgett, 2000). Immediately after crater formation,  $\sim$ 3.7 Ga (Deit et al., 2013; Tanaka et al., 2014; Thomson et al., 2011), the crater was infilled by fluvio-lacustrine sediments during an earlier wetter climate, followed by aeolian-dominated strata as conditions changed to a drier climate. After accumulation of the Mount Sharp group sequence was completed, there was a prolonged episode of aeolian exhumation, which removed as much as 2/3 of the crater fill, leaving proto-Mount Sharp at the center of Gale. Subsequent deposition followed this major aeolian deflation event, preserved in the overlying Siccar Point group (Watkins et al., 2022). The Aeolian Stimson formation, and the overlying Gediz Valis ridge are the only two stratigraphic units so far encountered in this group.

The floor of Gale crater consists of the Bradbury group, which is characterized by interstratified conglomerates and sandstones that overly the fluvio-lacustrine mudstones of the Yellowknife Bay formation (Grotzinger et al., 2015). The Mount Sharp group overlies the Bradbury group and consists of the Murray, Carolyn Shoemaker, and Mirador formations (e.g., Caravaca et al., 2022; Cardenas et al., 2023; Edgar et al., 2024; Fedo et al., 2022; Grotzinger et al., 2014; Meyer et al., 2024; Roberts et al., 2024; Stack et al., 2019; Vasavada, 2022). The Murray formation is primarily composed of laminated lacustrine mudstones and occasional cross-stratified sandstones (Rampe et al., 2017). After visiting Vera Rubin ridge (L. A. Edgar et al., 2020), an erosion-resistant

TRUSSELL ET AL. 2 of 17

21699100, 2025, 10, Downloaded from https://agupubs.onlinelibrary.wiley.com/doi/10.1029/2025/E009244 by Cochrane France, Wiley Online Library on [17/10/2025]. See the Terms

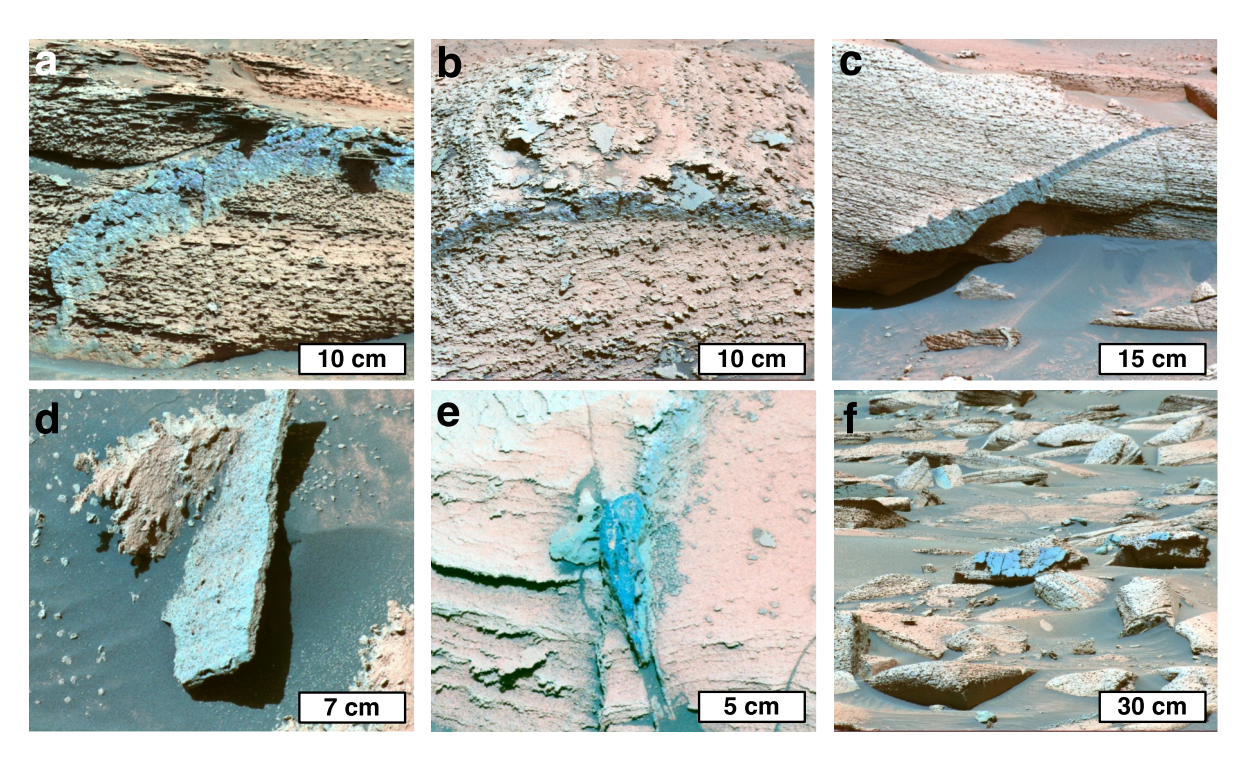


**Figure 1.** Mastcam enhanced Bayer-filter color images of dark-toned veins observed in the Chenapau Member. (a) Charvein, mcam04039, sol 3824. (b) Jardinopolis, mcam04065, sol 3830. (c) Kamani Kreek, mcam04120, sol 3842. (d) Crique Guillaume, mcam04259, sol 3865. (e) Mega Spilaio, mcam04314, sol 3873. (f) Samos, mcam04515, sol 3906. Vein heights are reported in Table 1. Image credit: NASA/JPL-Caltech/MSSS.

ridge enriched in hematite, the rover traversed south to the phyllosilicate-enriched Glen Torridon region (Bennett et al., 2023). Within the Glen Torridon region, the contact between the upper Murray and Carolyn Shoemaker formations is characterized by a transition from the lake-margin deposits to fluvial interstratified sandstones and mudstones (Fedo et al., 2022). The Carolyn Shoemaker formation is separated from the start of the Mirador formation by a shallow erosional unconformity (Meyer et al., 2024). The lower Mirador formation contains meter-scale cross-bedded sandstones, marking a transition to a drier environment dominated using aeolian processes (Caravaca et al., 2023; L. Edgar et al., 2024; Meyer et al., 2024).

The clay-sulfate transition begins in the Mercou member of the Carolyn Shoemaker formation and continues until the Amapari member of the Mirador formation. The clay-sulfate transition is characterized by a change from enrichment in phyllosilicates to hydrated amorphous Mg-sulfates (Chipera et al., 2023; Meyer et al., 2024; Rampe et al., 2022). On Sol 3560 (10 August 2022), Curiosity entered Marker Band Valley, the designated start of the layered sulfate-bearing unit (Roberts et al., 2023). The Chenapau member overlies the Amapari Marker Band, a laminated and resistant unit made of high-Ca pyroxene that marks the start of the layered sulfate-bearing unit (Figure 2) (Gasda et al., 2024; Mondro et al., 2025). The Chenapau member is characterized by shallow, planar bedding and pale, laminated bedrock bearing nodules and dark-toned materials (O'Connell-Cooper et al., 2024; Roberts et al., 2024). Alpha Particle X-ray Spectrometer (APXS) measurements in the Chenapau member show enrichment in MgO, SO<sub>3</sub>, and CaO relative to the mean Mount Sharp group, and Na enrichment similar to the Mount Sharp group but more abundant (O'Connell-Cooper et al., 2025). While exploring the Chenapau member of the Mirador formation, Curiosity encountered a set of dark-toned fracture filling materials between Sols 3824 and 3912 (Figure S1 in Supporting Information S1). Only one dark-toned vein, Kythira, was measured by APXS, which has 13.17 wt.% Na<sub>2</sub>O and 19.75 wt.% Cl (O'Connell-Cooper et al., 2025). These dark-toned fracture fills occurred between the Ubajara (UB) and Sequoia (SQ) drill targets (Figure 2). Analyses of these drill targets reveal that both contain a significant amorphous phase, in addition to minor amounts of siderite and hydrated salts such as gypsum and starkeyite (Clark et al., 2024; Tutolo et al., 2025).

TRUSSELL ET AL. 3 of 17

21699100, 2025, 10, Downloaded from https://agupubs.onlinelibrary.wiley.com/doi/10.1029/2023IE009244 by Cochrane France, Wiley Online Library on [17/10/2025]. See the Terms

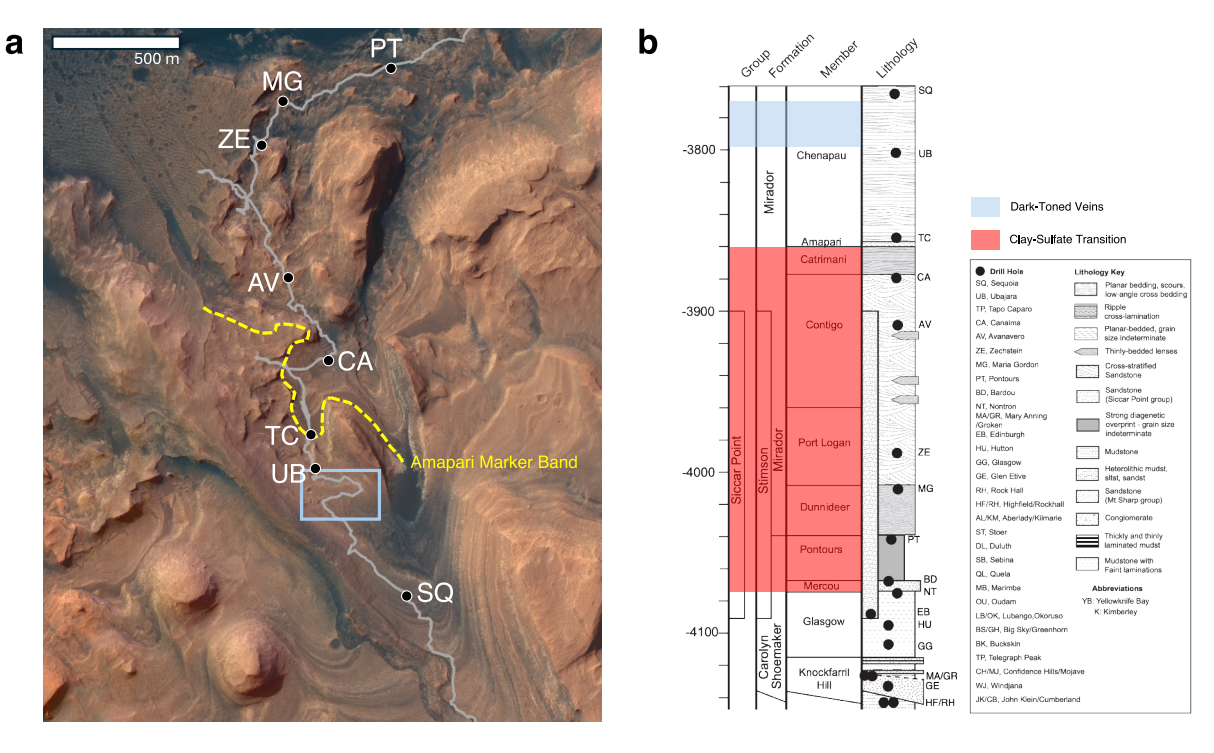


Figure 2. (a) Map of Curiosity's traverse (gray line) though the upper clay-sulfate transition and Amapari Marker Band (yellow line). The light blue box (Figure S1 in Supporting Information S1) marks the location of the dark-toned veins analyzed in this paper and the black circles indicate drill targets. Image credit: NASA/JPL/ University of Arizona (b) stratigraphic column of the Carolyn Shoemaker and Mirador Formations of the Mount Sharp Group, annotated to show the clay-sulfate transition (red) and occurrence of dark-toned veins (blue).

## 2.2. Previously Observed Veins

A variety of fracture-filling materials and veins were detected previously in Curiosity's mission, recording distinct post-emplacement aqueous events. For example, light-toned Ca-sulfate veins were observed throughout the Bradbury and Mount Sharp groups (De Toffoli et al., 2020; Kronyak et al., 2019; L'Haridon et al., 2018; Nachon et al., 2014). These Ca-sulfate veins are proposed to have formed initially as infilling of the Gale crater basin led to burial of sediments, allowing for overpressure of fluids and hydrofracture of the host rocks (De Toffoli et al., 2020). Gypsum deposited by sulfur-rich fluids along these fractures likely dehydrated to bassanite under later arid conditions (Rapin et al., 2016). In the Murray formation, some of these veins show an enrichment in Fe and Mg that indicates changing redox conditions in the fluids that interact with Gale crater stratigraphy (L'Haridon et al., 2018). In the Pahrump Hills member of the Murray formation, three types of veins were discovered: gray veins, light-toned veins, and dark-toned veins (Kronyak et al., 2019). The gray veins occurred as raised ridges with elevated Mg and Ca. Gray veins in this area also occurred along the edges of light-toned veins rich in Ca-sulfates, suggesting that sulfate fluids reutilized the same fractures (Kronyak et al., 2019; Nachon et al., 2017). Dark-toned veins occurred as smooth platy material enriched in Fe, K, and trace elements compared to the host rock, suggesting they formed under hydrothermal to mildly acidic conditions. In the clay-rich Glen Torridon region, dark-toned Fe and Mn veins may have formed during warmer, more reducing conditions created by hydrothermal fluids (Gasda et al., 2022).

#### 2.3. Previous Halite Detections

The presence of halite on Mars is significant because chloride salts are typically the last mineral to precipitate out of saline solutions, placing constraints on fluid chemistry and timing (Nachon et al., 2014; Tosca & McLennan, 2006). Compared to Earth, the abundance of basaltic weathering on Mars can buffer the acidity of sulfate solutions and favor the precipitation of carbonates and chlorides (Rapin et al., 2019; Tosca & McLennan, 2006). Throughout Curiosity's journey, chlorine has been detected at <3 wt.% Cl in rocks and soils

TRUSSELL ET AL. 4 of 17



Table 1
Mastcam Multispectral Images Used in Our Analysis of Dark-Toned Veins

Sol	Sequence	Target	Vein height (cm)
3824	mcam04039	Charvein	4.5–6
3830	mcam04065	Jardinopolis	0.7-2.6
3842	mcam04120	Kamani Kreek	1–5
3846	mcam04141	Crique Rubis	14–16
3856	mcam04196	Gorgona*	x
3865	mcam04259	Crique Guillaume	6–7.5
3873	mcam04314	Mega Spilaio	1.5–1.7
3887	mcam04395	Paros*	x
3906	mcam04515	Samos*	x

*Note.* \*Vein height measurements of "x" denote veins that we were unable to measure in 3D projections of Mastcam images due to their distance from the rover.

(Thomas et al., 2019). In the Murray formation, Na and Cl enrichment consistent with halite were limited to along the margins of Ca-sulfate veins and isolated grains (~15 wt.% NaCl) in rocks (Thomas et al., 2019). Due to halite's high solubility and the sporadic occurrence of halite in this unit, these salts are interpreted to have formed by late-stage Ca-sulfate fluids that dissolved primary evaporitic deposits of halite and mobilized Na and Cl ions (Rapin et al., 2019; Schwenzer et al., 2016; Thomas et al., 2019). These saline fluids later precipitated along fractures, leading to the deposition of Ca-sulfate veins with halite at their margins (Thomas et al., 2019). Upon entering the sulfate unit, detections consistent with halite increased significantly (up to 35 wt.% NaCl) and began to occur as contiguous laminae (Berger et al., 2023; Meslin et al., 2022, 2024; O'Connell-Cooper et al., 2024). Some of these halite-rich laminae are even crosscut by Ca-sulfate veins, suggesting that they were not dissolved by later calcium-sulfate fluids (Meslin et al., 2024). These halite-rich features may have formed by the dissolution and reprecipitation of primary evaporitic beds and likely represent a more arid period in Gale crater's history (Meslin et al., 2024).

#### 3. Methods

#### 3.1. Mastcam Spectra: Collection and Analysis

The Mast Camera (Mastcam) instrument on Curiosity consists of two charge-coupled device (CCD) cameras with different focal lengths (34 and 100 mm) that can acquire stereo and multispectral images over a broad field of view surrounding the rover (Bell et al., 2017; Malin et al., 2017). Each camera includes an eight-position filter wheel allowing for multispectral imaging and the creation of calibrated reflectance spectra in 12 unique wavelengths from ~400 to 1,100 nm (Bell et al., 2017). Mastcam cannot unequivocally identify minerals, but this wavelength range can constrain the oxidation state and hydration of iron-bearing phases in rocks and soils (Rice et al., 2022). We identified nine dark-toned veins in Mastcam multispectral images (Table 1) from sols 3824 to 3906. For each vein, we created color-composite, and decorrelation stretch (DCS) images (Gillespie et al., 1986) using the right-eye filters R6 (1,013 nm), R1 (527 nm), and R2 (447 nm) and left-eye filters L6 (1,012 nm), L1 (527 nm), and L2 (445 nm). We analyzed veins in color composite images to characterize vein morphology, texture, and relation to the host rock. Mastcam multispectral images were calibrated from radiance (I) to radiance factor (I/F) (relative reflectance) using images of the Mastcam calibration target (caltarget) (Bell et al., 2017; Wellington et al., 2017). The caltarget consists of three grayscale rings with known reflectance properties, from which polygonal regions of interest (ROIs) are selected while avoiding dust and shadows on the rings. The radiance values from the ROIs of each ring are then corrected for illumination, viewing geometry, and dust deposition according to the calibration pipeline outlined by Bell et al. (2017). The slope of the best-fine line passing through the average radiance values for each of the three rings is used to determine the calibration coefficient. The radiance factor is then divided by the cosine of the solar incidence angle to obtain the relative reflectance. For each calibrated set of multispectral images, we selected ROIs from the veins, host rocks, and surrounding soils/sands where available. ROIs were manually selected by inspecting images to locate regions on veins and host rocks that were spectrally uniform, consistent in texture, and free of shadows or steep edges. We scaled spectra from the left eye to the right eye at 1,013 nm and then averaged spectra for both eyes to obtain a 12wavelength spectrum per ROI. Then, we calculated spectral parameters and band ratios for each spectra obtained using formulas from Rice et al., 2010, 2022 (Table 2).

### 3.2. 3D Analysis of Vein Morphology and Texture

We used the Planetary Robotics 3D Viewer (Pro3D) software to visualize Mastcam stereo images and mosaics of the veins in 3D (Paar et al., 2023). The Planetary Robotics Vision Processing Framework (PRoVIP) pipeline (Traxler et al., 2022) uses stereo matching and mosaicking to create a single spherically projected Ortho and distance map for each Mastcam scene. Rover localization data is used to perform a SPICE-based transform into a Mars geographic coordinate frame and the resulting regular textured mesh is converted to ordered point clouds (OPCs) that are optimized for use in the PRo3D. Viewing the OPCs in Pro3D allows for the spatially consistent

TRUSSELL ET AL. 5 of 17

Table 2
Mastcam Spectral Parameters Calculated for Veins, Host Rocks, and Sands (Rice et al., 2022)

Mastcam parameter	Formula	Description	
527 nm (L1) band depth	$1 - \frac{R_{527}}{0.645R_{445} + 0.335R_{676}}$	Higher values indicate greater Fe oxidation	
751 nm (L3)/445 nm (L2) ratio	$R_{751}/R_{445}$	Red/blue ratio; higher values indicate greater Fe oxidation	
867 nm (L5) band depth	$1 - \frac{R_{867}}{0.556R_{751} + 0.444R_{1012}}$	Higher values indicate crystalline hematite; negative values consistent with olivine or pyroxene	
805 nm (R3)/937 nm (R5) ratio	$R_{805}/R_{937}$	Higher values associated with broad Fe absorptions in NIR	
937 nm (R5)/1,013 nm (R6) ratio	$R_{937}/R_{1013}$	Higher values with a flat NIR profile are consistent with a hydration band at 980 nm; higher values with larger 805 nm/937 nm ratios consistent with ferrous absorptions by olivine or	
		pyroxene	

placement of scale bars and lines in various projection modes, as well as measurements including thicknesses and slopes.

We analyzed 3D reconstructions of the veins in this study to characterize their morphologies, textures, and relationships to their respective host rocks. Compared to 2D analysis, 3D reconstruction of the veins allows for the quantification of vein orientations, including strike and dip. Additionally, 3D reconstructions facilitate the visualization of host rock bedding and vein relief, providing insights into the stress regime and mechanics of fracture formation. In Pro3D, we also measured the heights of the veins by drawing a vertical line annotation with a linear projection between the base and top of the vein. For veins that were sufficiently close to the rover, vein heights were measured in multiple regions across the length of the vein, providing a minimum and maximum height.

#### 3.3. ChemCam Active and Passive Measurements

The ChemCam instrument on Curiosity uses laser-induced breakdown spectroscopy (LIBS) to provide elemental compositions of rock and soil targets located mostly within 4.5 m of the rover (Maurice et al., 2012; Wiens et al., 2012). In active mode, ChemCam uses a 1,067 nm laser to ablate a linear array of typically five points on a given target with a spacing of 1–2 mrad and 350–550-micron spot size (Maurice et al., 2016; Wiens et al., 2015). The emission spectrum of the generated plasma was then measured by ChemCam's 3 spectrometers that cover a wavelength range of 240–342 nm (UV), 382–469 nm (VIO), and 474–906 nm (VNIR) (Wiens et al., 2012, 2013). For each point in an array, ChemCam's laser fires 30 shots, where the first 5 shots are used to remove dust and omitted from calculations of chemistry. The remaining 25 shots were then averaged to estimate wt. % elemental composition using a multivariate model (Clegg et al., 2017). ChemCam also contains a remote-micro imager (RMI) that is used to image the context surrounding LIBS observation points (Le Mouélic et al., 2015). We identified 7 dark-toned veins targeted by ChemCam (including 2 not targeted by Mastcam) and analyzed their elemental chemistry to constrain vein composition and variations as a supplement to our Mastcam analyses (Table 3). We reviewed RMI images to distinguish points that fell on veins and points that fell on the host rock material adjacent to the veins (Figure 8).

Table 3
ChemCam Measurements of Veins and Corresponding Mastcam R0 Images

Sol	ChemCam sequence	Mastcam sequence	Target	Range (m)
3830	ccam01830	mcam04065	Jardinopolis	3.91
3831	ccam01831	mcam04071	Sunsas (Charvein)	4.10
3834	ccam01834	mcam04081	Jutica (Jardinopolis Extension)	3.97
3836	ccam04834	mcam04089	Walterlandia	3.90
3842	ccam03841	mcam04122	Sotara	4.04
3851	ccam01851	mcam04173	Calafate (Crique Rubis)	3.29
3873	ccam01873	mcam04318	Mega Spilaio	2.84

TRUSSELL ET AL. 6 of 17

21699100, 2025, 10, Downloaded from https://agupubs.onlin

Wiley Online Library on [17/10/2025]. See the Terms and Conditions (https://onlinelibrary.wiley.com/terms-

and-conditions) on Wiley Online Library for rules of use; OA articles are governed by the applicable Creatiw

ChemCam parameter	Formula	Description	
535 nm band depth (BD535)	$1 - \frac{R_{535}}{0.65R_{500} + 0.35R_{600}}$	Higher values indicate greater Fe oxidation	
Slope from 750 to 840 nm (S7584)	$\frac{R_{840} - R_{750}}{840 - 750}$	NIR slope; negative values indicate a downturn consistent with broad Fe <sup>2+</sup> absorptions from olivine or pyroxene or ferric absorptions around 860 nm	

ChemCam cannot directly determine mineralogy, but the mineralogy can be inferred by fitting the emission peaks for different elements and correlating them. Prior to peak fitting, we normalized the spectra using the ChemCam Norm 3 method of dividing the spectra by the sum of the intensities in the VNIR detector (Thomas et al., 2018). We used a skewed Voigt approximation that is a product of the Lorentzian and Gaussian functions to fit the Cl peak centered at 837.8 nm and the Na doublet centered at 819 nm. In order to determine the peak area of the Na doublet, we fit the individual Na peaks at 818.6 and 819.8 nm and summed their areas. For each normalized peak, the local continuum was removed by fitting a second order polynomial to the local minima on each side of the peak and subtracting this baseline. Then, we used a nonlinear least squares optimization to minimize the residual between the continuum-removed normalized spectrum and the fitted profile. The peak area for each line was then estimated by multiplying the height of the fitted peak by the full width at half maximum. We then plotted the normalized Na versus normalized Cl peak areas and fit a linear regression to the data.

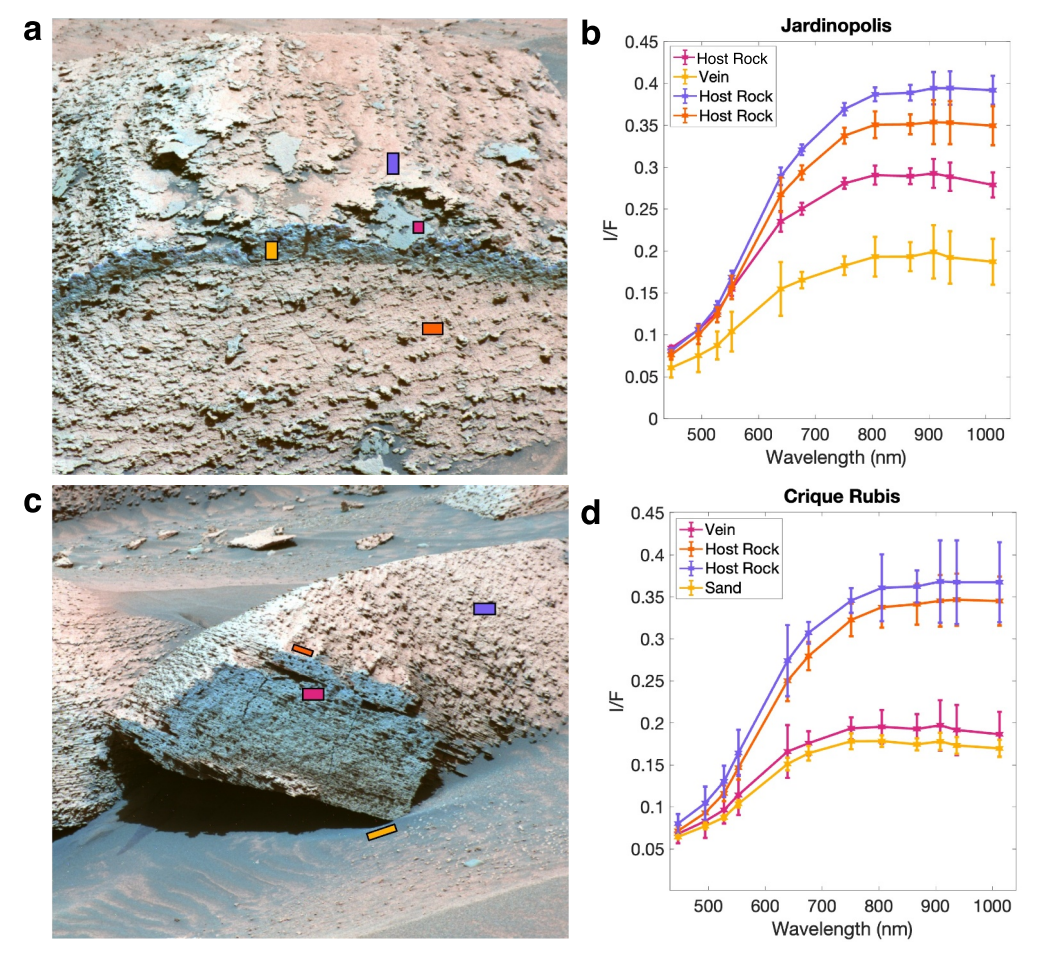


**Figure 3.** (a) ROI selections for Jardinopolis on a Mastcam color-composite image (mcam04073). (b) Corresponding Mastcam spectra for selections in panel (a). (c) ROI selections for Crique Rubis on a Mastcam color-composite image (mcam04141). (d) Corresponding Mastcam spectra for selections in panel (c).

TRUSSELL ET AL. 7 of 17

21699100, 2025, 10, Downloaded from https://agupubs.onlinelibrary.wiley.com/doi/10.1029/2025IE009244 by Cochrane France, Wiley Online Library on [17/10/2025]. See

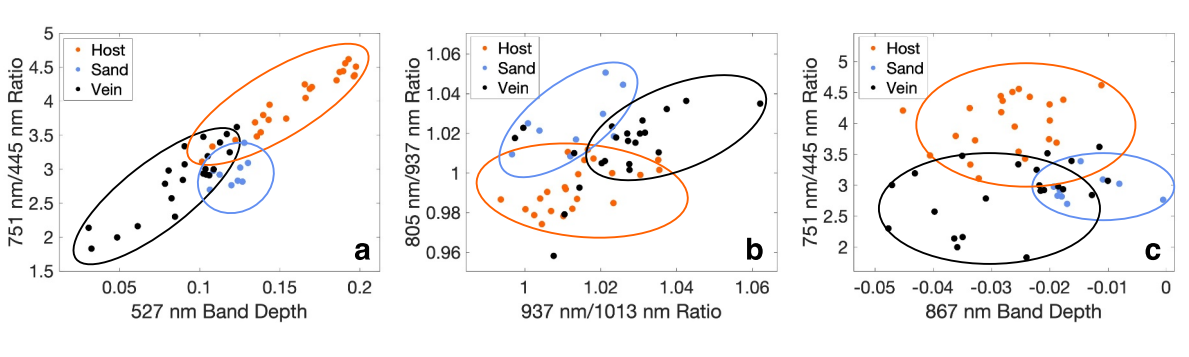


Figure 4. Comparison of Mastcam spectral parameters for veins (black), host rocks (orange), and surrounding sands (blue). (a) 751 nm/445 nm ratio versus 527 nm band depth. (b) 805/937 nm ratio versus 937/1,013 nm ratio. (c) 751 nm/445 m ratio versus 867 nm band depth.

ChemCam also has a passive mode where passive reflected solar radiance spectra are acquired after each LIBS observation, enabling the creation of calibrated visible to near-infrared relative reflectance spectra from 400 to 840 nm on a dust-removed surface (Johnson et al., 2015). We reviewed ChemCam passive spectra for the darktoned veins in Table 3 as a complement to the Mastcam spectra analyzed. ChemCam passive spectra cover a wavelength range that also allows for the identification of iron oxides and oxyhydroxides at a higher spectral resolution than Mastcam, making this data set a good choice for detailed spectral analysis of veins. However, ChemCam passive spectra are limited to the 0.65-mrad field-of-view (Johnson et al., 2015), that is a 2.275 mm spot size at 3.5 m, whereas Mastcam acquires a larger scene including the host rocks, veins, and surrounding materials (Fraeman et al., 2020).

We applied a Savitzky-Golay filter with a window length of 51 channels to smooth the passive spectra and enable the distinction between spectral features and noise (Manelski et al., 2023). This window length corresponds to a width of  $\sim$ 4–8 nm, optimizing the detection of spectral features associated with broader crystal field transitions and Fe absorptions. We calculated ChemCam spectral parameters for points that fell on the veins and host rocks using the formulas from Manelski et al., 2023 (Table 4). We calculated these parameters both for points that fell on the dark-toned veins and for all veins previously measured by ChemCam between sols 0 and 4133. The albedo of ChemCam passive spectra was estimated using the average reflectance across the entire spectral range.

## 4. Results

### 4.1. Mastcam Results

Mastcam spectra of the veins, host rocks, and nearby sands all exhibit a steep positive-sloping ferric absorption edge followed by a gentle negative-sloping NIR profile (Figure 3). The dark-toned veins in this study display a weak downturn in the Mastcam long-wavelength filters, from ~750 to 1,000 nm (Figures 3b and 3d). This downturn is pronounced in the last two Mastcam filters, from 937 to 1,013 nm. Host rock spectra also display a similar downturn; however, the degree of this downturn is weaker than the one observed in the veins. Some veins, host rock and sands exhibit a slight absorption at 867 nm in Mastcam spectra that may be attributed to the presence of hematite (Figure 3). Compared to their host rocks, veins generally exhibit a weaker 527 nm band depth and lower 751/445 nm ratios (Figure 4a). Veins also have a slightly higher 937/1,013 nm ratio and higher 805/937 nm ratio than their host rocks (Figure 4b). Veins exhibit greater variability in these parameters than host rocks and sands, especially for those derived from wavelengths >750 nm. We attribute this variability to compositional differences within the veins which incorporate varying fractions of ferrous material from the host rock. We do not interpret the increased variability as an albedo effect since sands also have low albedo but do not display as much variability. Veins, host rocks, and sand all display negative 867 nm band depths and host rocks display higher 751/445 nm ratios than veins and sands (Figure 4c).

In Mastcam color composite images, veins appear as dark-toned, linear, fracture-fills or platy to fin-like sheets that are distinct in color from the host rock (Figure 5). The host rocks display a laminated, nodular to flakey morphology and parallel/horizontal bedding. In right-eye DCS images, veins appear blue to green while the host rock appears redder (Figure S2 in Supporting Information S1). The veins generally exhibit sub-horizontal to

TRUSSELL ET AL. 8 of 17

21699100, 2025, 10, Downloaded from https://agupubs.onlinelibrary.wiley.com/doi/10.1029/2025JE009244 by Cochrane France, Wiley Online Library on [17/10/2025]. See

ns) on Wiley Online Library for rules of use; OA articles are governed by the applicable Creati

**Figure 5.** Portions of Mastcam color-composite images of dark-toned veins and host rocks. White arrows indicate fractures that occur perpendicular to the veins. (a) Jardinopolis, mcam04065, crosscuts a host rock with a flakey morphology. (b) Charvein, mcam04039, exhibits a nodular texture and crosscuts the laminated horizontal bedding in the host rock.

horizontal orientations relative to the host rock laminations, but in some examples (e.g., Mega Spilaio and Gorgona) form vertical sheets. The veins are straight to slightly arcuate in shape and occur in isolation (i.e., they do not exhibit branching or form networks). In some cases (e.g., Charvein, Kamani Kreek, Crique Rubis), the textures of the veins appear slightly nodular or laminated, resembling that of the surrounding host rock. In other cases, the veins appear smooth or slightly pitted (e.g., Paros, Mega Silaio). The host rocks surrounding the veins contain visible fractures oriented perpendicular to the vein fracture (Figure 5). These perpendicular cracks lack vein or mineral infill and, in some cases, cut through the veins, indicating that they formed later. The perpendicular direction of the cracks also suggests that the rock may have experienced a different stress regime post-vein emplacement.

## 4.2. PRo3D Results

In 3D reconstructions of Mastcam stereo images and mosaics, the veins have positive relief appearing as linear ridges or resistant edges that protrude from the host rock (Figure 6). In some cases, the nodular to platy morphology of the host rock is clearly preserved within the vein itself (Figure 6a). The boundaries between the veins and host rocks are often uneven and rough, with some boundaries having a serrated appearance (Figure 6b). In one example, Kamani Kreek, the host rock below the vein appears recessed (Figure 6c). The veins generally

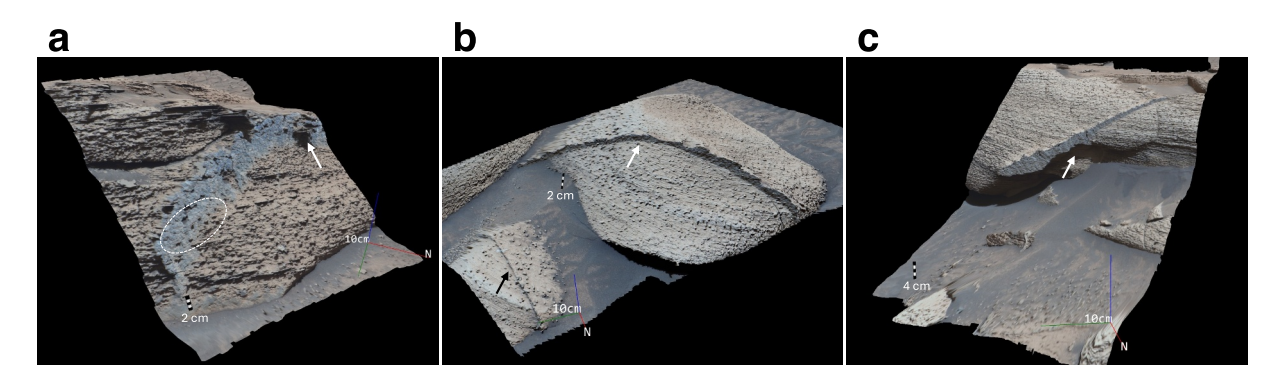


**Figure 6.** PRo3D reconstructions of Mastcam stereo images and mosaics. (a) Sol 3824 mcam04073 Charvein. Platy (white arrow) and nodular textures (white dashed ellipse) in the vein are also visible in the host rock. (b) Sol 3842 mcam04122 Sotara mosaic. Black arrow indicates a smaller narrow vein in the scene and white arrow shows a larger vein with serrated edges. (c) Sol 3842 mcam04120 Kamani Kreek. White arrow shows the recessed region of the host rock below the vein.

TRUSSELL ET AL. 9 of 17

21699100, 2025, 10, Downloa

Wiley Online Library on [17/10/2025]. See the Term:

of use; OA articles are governed by the applicable Crea

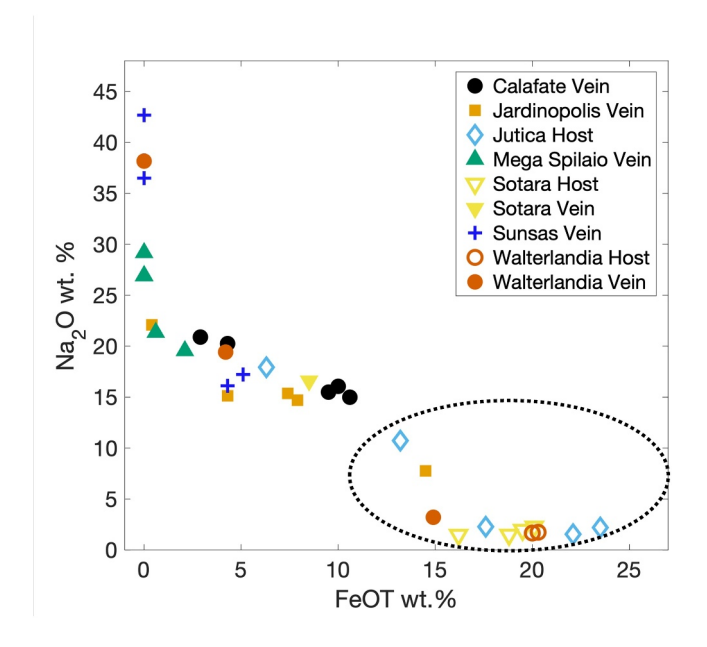


**Figure 7.** Na<sub>2</sub>O versus FeOT wt.% for dark-toned veins and their host rocks. Laser-induced breakdown spectroscopy points on dark-toned veins are indicated by closed symbols, while points on host rocks are indicated by open symbols. Black dashed ellipses indicate where the majority of host rocks plot.

have consistent heights throughout their lengths, with minimal variation between the minimum and maximum height of the vein (Table 1). In Mastcam mosaics, multiple veins can be seen in the same scene with veins often displaying a similar orientation and morphology to each other (Figure S3 in Supporting Information S1).

#### 4.3. ChemCam Active and Passive Results

ChemCam LIBS analysis of veins revealed a significant Na<sub>2</sub>O component (~10-42 wt.% Na<sub>2</sub>O). LIBS points that fall on the host rock immediately adjacent to veins display lower levels of 1.4-2.2 wt.% Na<sub>2</sub>O (Figure 7 and Figure S4 in Supporting Information S1). Host rocks have a significant MgO component ranging between 3.6 and 16.3 wt.% and a CaO component ranging between 0.4 and 15.9 wt.%. Dark-toned veins have lower levels ranging between 0.6 and 5.1 wt.% for MgO and 0-18.2 wt.% for CaO. Reported FeOT values (which do not distinguish between Fe<sup>2+</sup> and Fe<sup>3+</sup>) ranged from 6.3 to 23.5 wt.% and from 0 to 14.9 wt.% for host rocks and veins, respectively. Raster points that fall along the center of the veins exhibit the highest concentration of Na<sub>2</sub>O. Values of Na<sub>2</sub>O decrease toward the edge of the veins, whereas FeOT increases, consistent with dilution (Figure S5 in Supporting Information S1). There is a positive linear correlation between the normalized Na and Cl peak areas (Figure 8), possibly consistent with halite. The O and Cl emission line intensities are not correlated; therefore, it is unlikely that the observed correlation between Na and Cl is caused by chlorate or percolate (Meslin et al., 2024; Thomas et al., 2019).

ChemCam passive spectra of veins display lower relative reflectance values than their host rocks (Figure 9). Host rock spectra exhibit a steeper slope from 500 to 600 nm compared to veins. Host rocks and veins spectra both exhibit a reflectance maximum near ~750 nm and a slightly negative slope from 750 to 840 nm, in agreement with Mastcam spectra over the same observed wavelengths (Figure 3). Comparison of these veins with all veins measured by ChemCam between sols 0 and 4133 reveals that these veins have low albedos of 0.7–0.14, consistent with their dark-tone appearance (Figure 10b). These veins also displayed positive 535 nm band depths and weakly negative slopes from 750 to 840 nm (Figure 10a).

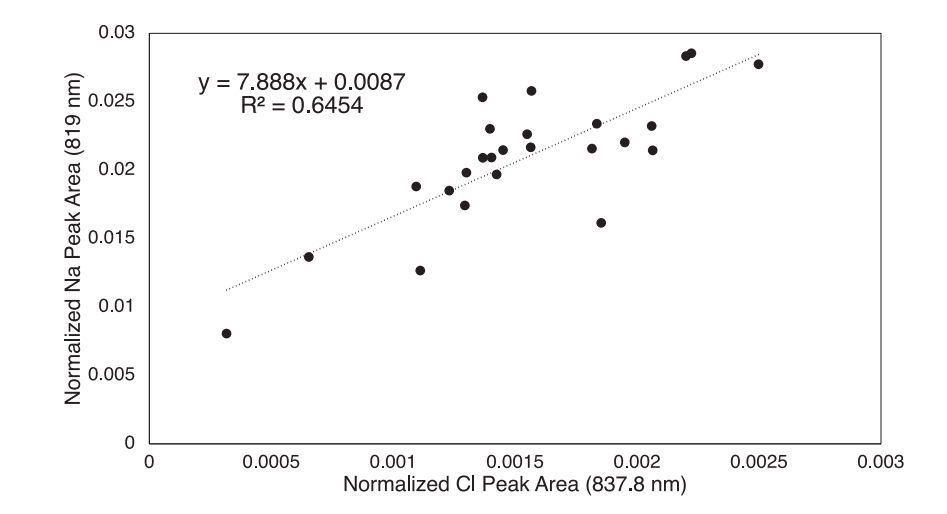


**Figure 8.** Normalized Cl peak area (837.8 nm) versus normalized Na peak area (819 nm) for ChemCam points on dark-toned veins. Black dashed line is the linear regression fit.

TRUSSELL ET AL. 10 of 17

21699100, 2025, 10, Downloaded from https://agupubs.onlinelibrary.wiley.com/doi/10.1029/2025JE009244 by Cochrane France, Wiley Online Library on [17/10/2025]. See the Terms and Conditions (http://agupubs.onlinelibrary.wiley.com/doi/10.1029/2025JE009244 by Cochrane France, Wiley Online Library on [17/10/2025]. See the Terms and Conditions (http://agupubs.onlinelibrary.wiley.com/doi/10.1029/2025JE009244 by Cochrane France, Wiley Online Library on [17/10/2025]. See the Terms and Conditions (http://agupubs.onlinelibrary.wiley.com/doi/10.1029/2025JE009244 by Cochrane France, Wiley Online Library on [17/10/2025].

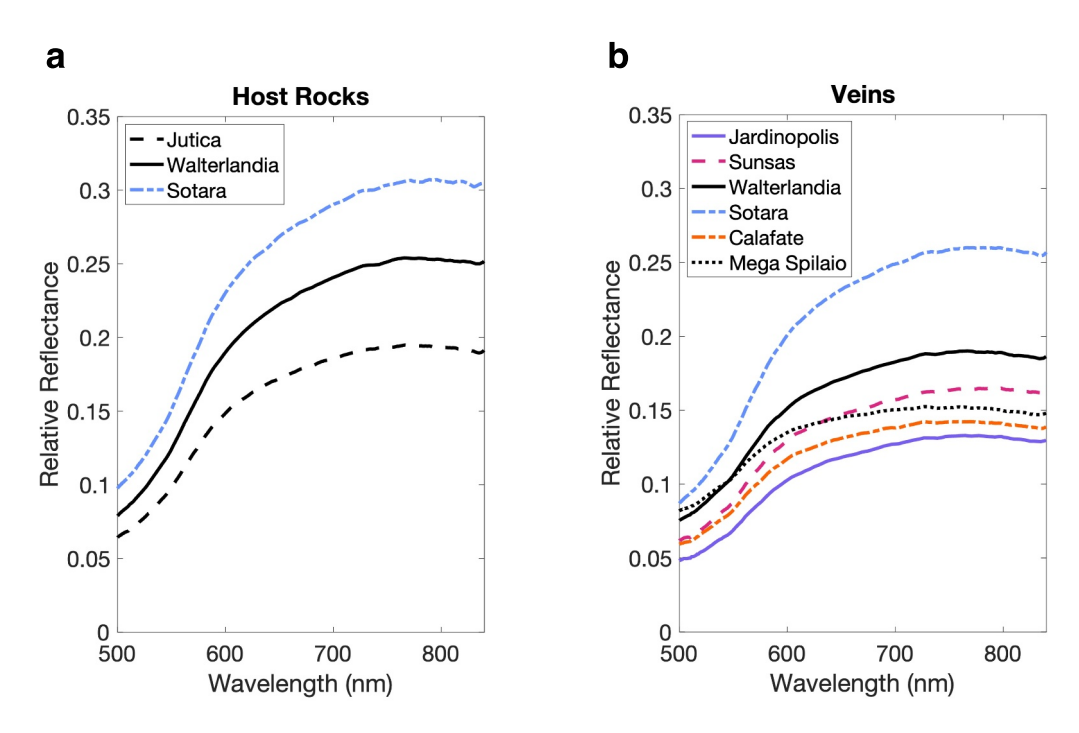


Figure 9. (a) ChemCam passive spectra of host rocks, Jutica (Sol 3834, ccam01834, Point 1), Walterlandia (Sol 3836, ccam04834, Point 4), and Sotara (Sol 3842, ccam03841, Point 1). (b) ChemCam passive spectra of dark-toned veins, Jardinopolis (Sol 3830, ccam01830, Point 1), Sunsas (Sol 3831, ccam01831, Point 1), Walterlandia (Sol 3836, ccam04834, Point 1), Sotara (Sol 3842, ccam03841, Point 4), Calafate (Sol 3851, ccam01851, Point 1), and Mega Spilaio (Sol 3873, ccam01873, Point 1).

## 5. Interpretations and Discussion

### 5.1. Evidence for Ferric and Ferrous Components in Veins

Both Mastcam spectra and ChemCam passive spectra of dark-toned veins and their host rocks exhibit a positive red slope from ~500 to 750 nm caused by the presence of ferric iron (Meslin et al., 2024; Thomas et al., 2019). ChemCam passive spectra exhibit weak 535 nm absorption bands consistent with the presence of (Fe<sup>3+</sup>) ferric iron (Figure 10b). Ferric iron may be exogeneous from Martian dust coating the surfaces of rocks, but the presence of this feature in dust-cleared ChemCam passive spectra (acquired after LIBS removed dust) favors an endogenic source of ferric iron within the rocks and veins. This ferric absorption edge is steeper for host rocks,

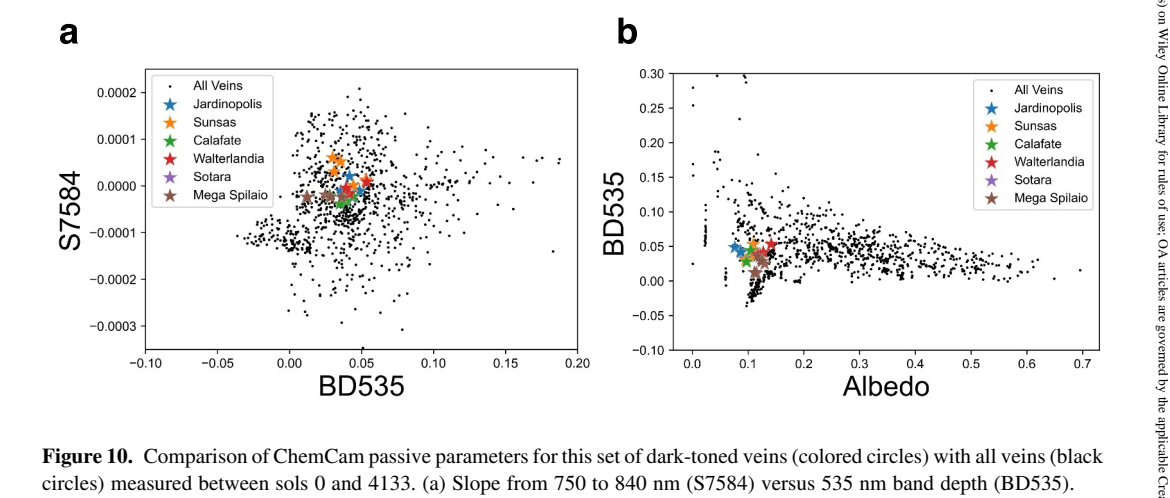


Figure 10. Comparison of ChemCam passive parameters for this set of dark-toned veins (colored circles) with all veins (black circles) measured between sols 0 and 4133. (a) Slope from 750 to 840 nm (S7584) versus 535 nm band depth (BD535). (b) 535 nm band depth (BD535) versus albedo.

TRUSSELL ET AL. 11 of 17



10.1029/2025JE009244

because of their redder color and increased brightness compared to the dark-toned veins. The steepness of the ferric absorption edge also increases with increasing oxidation or dust-coating of rocks (Bell et al., 2000; Johnson et al., 2015). Veins exhibit smaller 527 nm band depths and lower 751 nm/445 nm (Red/Blue) ratios compared to their host rocks, suggesting a lower degree of oxidation than their host rocks (Figure 4a) (Farrand et al., 2008; Rice et al., 2022). The 867 nm band depths observed for host rocks and veins are slightly negative, consistent with the convex NIR profile characteristic of ferrous materials including olivine and pyroxene (Horgan et al., 2020; Rice et al., 2022). Weak absorptions are visible near 867 nm in Figure 3 due to the presence of minor ferric oxide phases such as crystalline hematite, but the calculated 867 nm band depth is negative due to the general downturn in reflectance from 750 to 1,013 nm.

The most distinguishing feature of Mastcam spectra of veins and host rocks is the presence of a downturn or negative slope in the long-wavelength Mastcam filters from 750 to 1,013 nm (Figure 3). This downturn may be caused by a hydration signature around 1,000 nm when coupled with a flat NIR profile (Rice et al., 2010) or by the presence of ferrous iron in olivine or pyroxene (Rice et al., 2022). We observed that both dark-toned veins and host rocks exhibit large 805/937 nm ratios and large 937/1,013 nm ratios (<1.0), consistent with a broad absorption near 1,000 nm (Figure 4b). This downturn is unlikely to be caused by hydration because ChemCam LIBS points on veins lack a strong hydrogen peak at 656 nm (Figure S6 in Supporting Information S1). Additionally, the presence of even minor numbers of phyllosilicates and basalts can mask the hydration feature in Mastcam spectra (Eng et al., 2024). Instead, we favor that this downturn is caused by the presence of ferrous components such as olivine or pyroxene from basalt. ChemCam passive spectra of the veins and host rocks also display a weakly negative slope from 750 to 840 nm, consistent with broad absorptions near 1 micron due to ferrous iron (Figures 9 and 10a).

Fitting of the ChemCam Na and Cl peak intensities of the dark-toned veins shows a linear correlation suggestive of halite (Figure 8). However, halite is spectrally neutral in the VIS-NIR wavelength ranges observed by Mastcam spectra and ChemCam passive spectra (Crowley, 1991; Farrand et al., 2023). Thus, halite is not associated with the broad absorption observed in Mastcam spectra near 1,000 nm. ChemCam LIBS points also suggest that veins still contain a minor component of Fe, with points that fall directly on veins containing as much as 15 wt.% FeOT, whereas points on the surrounding host rock containing as much as 25 wt.% FeOT (Figure 7). The points with the highest wt.% Na are concentrated along the center of the veins, as exhibited by decreasing Na and increasing Fe as the distance from the center of the fracture increases (Figure S5 in Supporting Information S1). This is consistent with dilution of the primary haltie vein phase with the host rock material.

#### 5.2. Interpretation of Vein Formation

The composition of the dark-toned veins and their morphologies provide context into the nature of the fluids that formed these veins. Our results from analyses of Mastcam and ChemCam chemical/mineralogical data suggest that these dark-toned veins are enriched in Na and Cl, consistent with halite, and contain a minor basaltic component present as ferrous olivine or pyroxene. The gray, dark-toned color of the veins may be explained by the mixing of ferrous materials with the halite, as the veins are not composed of pure halite. The horizontal and vertical orientations of the dark-toned veins, as well as the perpendicular unfilled fractures indicate that these rocks experienced multiple stress regimes and periods of fluid flow.

We hypothesize that these veins formed through a multi-stage process consisting of the initial formation of the fractures followed by exhumation, halite precipitation, and differential erosion. Initially, sedimentary layers in Gale crater were buried and compacted by overlying materials leading to lithification of the sedimentary layers and the trapping of fluids in open pore spaces. These fluids may have been the source brine for the sulfates and carbonates in the sulfate-bearing unit, possibly derived from a regional groundwater system (Seeger & Grotzinger, 2024; Tutolo et al., 2025). As the overburden pressure from the overlying rock increased, these trapped fluids were over pressurized, eventually overcoming the tensile strength of the rock and leading to hydraulic fracturing. The hydraulic fracturing origin is consistent with the horizontal and vertical orientations of the fractures. These orientations indicate that the rocks experienced a significant vertical stress load that led to fracture along the weaker laminated bedding planes in the rock.

TRUSSELL ET AL. 12 of 17

21699100, 2025, 10, Downl

At a later time, these fractured rocks were exhumed to the near surface where Na- and Cl-bearing fluids infiltrated the pre-existing fracture network. These saline fluids, concentrated through burial and evaporation, may have evolved from the same brine that produced siderites and sulfates observed throughout the same unit, as such a brine was likely long-lived and regionally extensive (Tutolo et al., 2025). Alternatively, these saline fluids may have been derived from a later brine that is distinct from the one responsible for the siderites and sulfates. Halite within this unit is mostly limited to diagenetic features such as veins and platy laminations, whereas siderites and sulfates occur as cement throughout the bedrock, suggesting that the fluids responsible for halite precipitation were introduced post-lithification and represent the latest stages of fluid activity.

These saline fluids precipitated halite within the fractures and permeated a small degree into the surrounding host rock. This interpretation is supported by the observation that halite concentrations are strongest at the center of the veins and decrease toward the boundary between the vein and host rock material, consistent with the infiltration of saline fluids into the host rock. Differential erosion then led to the preservation of the rocks containing the dark-toned veins, as halite cemented the surrounding host rock. Mastcam images display clear evidence of platy and nodular host rock material being preserved within the veins (Figure 6). The positive-relief of the veins suggests that vein-forming fluids cemented the host rock material leading to the formation of erosion-resistant edges.

The formation of these veins though hydraulic fracturing is consistent with hypotheses for the formation of Casulfate veins observed earlier in the mission (Banham et al., 2025; Caswell & Milliken, 2017; Cosgrove et al., 2022). However, the composition of these veins is unique from previous veins in that they are enriched in halite mixed with host rock material. While Curiosity has detected halite previously in its traverse, these detections were limited to sporadic occurrences as isolated grains or along the edges of existing Ca-sulfate veins (Meslin et al., 2024). The presence of halite as a major vein-filling component suggests a distinct fluid flow event linked to the remobilization of evaporite assemblages or the precipitation of salts from evolving brine solutions. The preservation of these veins implies that conditions have remained arid since their formation, as halite is highly soluble and typically the last mineral to crystallize from an evaporating brine. Halite can also trap fluid inclusions and form crusts that protect organisms from radiation (Gómez et al., 2012), making halite-rich features a possible target for biosignature detection.

## 6. Conclusion

Our results present a new class of dark-toned veins in Gale crater that contain halite that permeated into fractures and preserved host rock material. These veins are significant because they contain the first detection of halite in contiguous fractures on Mars (Meslin et al., 2024) and have a distinctive composition from previous veins observed in Curiosity's mission. The preservation of a ferrous component from the host rock within the veins suggests that these veins formed as saline fluids infiltrated fractures and permeated into the surrounding host rock material. Notably, the halite in these veins may have come from remobilization of evaporite deposits or precipitation of brines, signifying that Mars experienced a period of continued fluid stability even while the planet experienced a global transition to a more arid climate, consistent with other observations by Curiosity (Clark et al., 2024; Rapin et al., 2021, 2023; Stein et al., 2018). Future studies and rover operations should continue to target veins for their ability to record how fluid chemistries have changed throughout Mars's history.

#### **Conflict of Interest**

The authors declare no conflicts of interest relevant to this study.

## **Data Availability Statement**

The Mastcam images and multispectral data used in this manuscript are available on the Planetary Data System (PDS) Cartography and Imaging Sciences Node (Planetary Data System Cartography and Imaging Sciences Node, 2025). The ChemCam active and passive data used in this manuscript are available on the PDS Geosciences node (Planetary Data System Geosciences Node, 2025). Additional data, including the Mastcam ROI selections and ChemCam peak fitting scripts can be found in a Zenodo repository (Trussell, 2025).

TRUSSELL ET AL. 13 of 17



10.1029/2025JE009244

#### Acknowledgments

Thank you to the Malin Space Science Systems and MSL operations teams that enabled the collection of these data sets. and to the Arizona State University students and staff that helped with Mastcam calibrations. This research was funded by the NASA MSL Project, via subcontract 11-0124 to Arizona State University from Malin Space Sciences, Inc. This material is based upon work supported by the National Science Foundation Graduate Research Fellowship under Grant 2233001. Any opinion, findings, and conclusions or recommendations expressed in this material are those of the authors(s) and do not necessarily reflect the views of the National Science Foundation, Part of the research was carried out at the Jet Propulsion Laboratory, California Institute of Technology, under a contract with the National Aeronautics and Space Administration (80NM0018D0004).

#### References

- Banham, S. G., Cosgrove, J. W., Paar, G., Gupta, S., Hughes, M. N., Grant, J. A., et al. (2025). A burial history of the sedimentary succession preserved in Aeolis Mons, as recorded by fracture networks at Maria Gordon notch, Gale crater, Mars. *Journal of Geophysical Research: Planets*. 130(7), e2024JE008843. https://doi.org/10.1029/2024JE008843
- Banham, S. G., Gupta, S., Rubin, D. M., Watkins, J. A., Sumner, D. Y., Edgett, K. S., et al. (2018). Ancient Martian aeolian processes and palaeomorphology reconstructed from the Stimson formation on the lower slope of Aeolis Mons, Gale crater, Mars. *Sedimentology*, 65(4), 993–1042. https://doi.org/10.1111/sed.12469
- Banham, S. G., Roberts, A. L., Gupta, S., Davis, J. M., Thompson, L. M., Rubin, D. M., et al. (2024). Ice? Salt? Pressure? Sediment deformation structures as evidence of late-stage shallow groundwater in Gale crater, Mars. *Geology*, 52(7), 492–496. https://doi.org/10.1130/G51849.1
- Bell, J. F., Godber, A., McNair, S., Caplinger, M. A., Maki, J. N., Lemmon, M. T., et al. (2017). The Mars Science Laboratory Curiosity rover Mastcam instruments: Preflight and in-flight calibration, validation, and data archiving. Earth and Space Science, 4(7), 396–452. https://doi. org/10.1002/2016EA000219
- Bell, J. F., McSween, H. Y., Jr., Crisp, J. A., Morris, R. V., Murchie, S. L., Bridges, N. T., et al. (2000). Mineralogic and compositional properties of Martian soil and dust: Results from Mars Pathfinder. *Journal of Geophysical Research*, 105(E1), 1721–1755. https://doi.org/10.1029/
- Bennett, K. A., Fox, V. K., Bryk, A., Dietrich, W., Fedo, C., Edgar, L., et al. (2023). The Curiosity rover's exploration of Glen Torridon, Gale crater, Mars: An overview of the campaign and scientific results. *Journal of Geophysical Research: Planets*, 128(1), e2022JE007185. https://doi.org/10.1029/2022JE007185
- Berger, J. A., Gellert, R., McCraig, M. A., O'Connell-Cooper, C. D., Spray, J. G., Thompson, L. M., et al. (2023). Isochemical characteristics of the clay-sulfate transition in Gale crater, Mars: APXS results from Mont Mercou to the Marker Band Valley. In 54th Lunar and Planetary Science Conference.
- Bibring, J.-P., Langevin, Y., Mustard, J. F., Poulet, F., Arvidson, R., Gendrin, A., & Gondet, B. (2006). Global mineralogical and aqueous Mars history derived from OMEGA/Mars Express data. Science, 312(5772), 400–404. https://doi.org/10.1126/science.1122659
- Bishop, J. L., & Rampe, E. B. (2016). Evidence for a changing Martian climate from the mineralogy at Mawrth Vallis. *Earth and Planetary Science Letters*, 448, 42–48. https://doi.org/10.1016/j.epsl.2016.04.031
- Caravaca, G., Gupta, S., Mangold, N., Rapin, W., Schieber, J., Davis, J. M., et al. (2023). Still flowing: The fluvial structures of the Prow outcrop in the arid lower sulfate unit of Gale crater (Mars). In *International Conference on Fluvial Sedimentology* 2023. Retrieved from https://hal. science/hal-04052777
- Caravaca, G., Mangold, N., Dehouck, E., Schieber, J., Zaugg, L., Bryk, A. B., et al. (2022). From lake to river: Documenting an environmental transition across the Jura/Knockfarril Hill members boundary in the Glen Torridon region of Gale crater (Mars). *Journal of Geophysical Research: Planets*, 127(9), e2021JE007093. https://doi.org/10.1029/2021JE007093
- Cardenas, B. T., Grotzinger, J. P., Lamb, M. P., Lewis, K. W., Fedo, C. M., Bryk, A. B., et al. (2023). Barform deposits of the Carolyn Shoemaker formation, Gale crater, Mars. *Journal of Sedimentary Research*, 92(12), 1071–1092. https://doi.org/10.2110/jsr.2022.032
- Caswell, T. E., & Milliken, R. E. (2017). Evidence for hydraulic fracturing at Gale crater, Mars: Implications for burial depth of the Yellowknife Bay formation. Earth and Planetary Science Letters, 468, 72–84. https://doi.org/10.1016/j.epsl.2017.03.033
- Chipera, S. J., Vaniman, D. T., Rampe, E. B., Bristow, T. F., Martínez, G., Tu, V. M., et al. (2023). Mineralogical investigation of Mg-sulfate at the Canaima drill site, Gale crater, Mars. *Journal of Geophysical Research: Planets*, 128(11), e2023JE008041. https://doi.org/10.1029/2023JE008041
- Clark, J. V., Sutter, B., Mcadam, A., Archer, P. D., Lewis, J., Franz, H., et al. (2024). Changes in volatile mineralogy from the Marker Band Valley to the layered sulfate-bearing unit in Gale Crater, Mars: Results from the sample analysis at mars-evolved gas analyzer instrument. In 55th Lunar and Planetary Science Conference. Retrieved from https://insu.hal.science/insu-04543091
- Clegg, S. M., Wiens, R. C., Anderson, R., Forni, O., Frydenvang, J., Lasue, J., et al. (2017). Recalibration of the Mars Science Laboratory ChemCam instrument with an expanded geochemical database. Spectrochimica Acta Part B: Atomic Spectroscopy, 129, 64–85. https://doi.org/ 10.1016/j.sab.2016.12.003
- Cosgrove, J. W., Banham, S. G., Gupta, S., & Barnes, R. (2022). The origin of the fracture networks in the mudstones of Gale crater Mars; their implications regarding the state of stress and fluid pressure during their formation and the depth to which they were buried. *Journal of Geophysical Research: Planets*, 127(12), e2022JE007313. https://doi.org/10.1029/2022JE007313
- Crowley, J. K. (1991). Visible and near-infrared (0.4–2.5 µm) reflectance spectra of Playa evaporite minerals. *Journal of Geophysical Research*, 96(B10), 16231–16240. https://doi.org/10.1029/91JB01714
- Deit, L. L., Hauber, E., Fueten, F., Pondrelli, M., Rossi, A. P., & Jaumann, R. (2013). Sequence of infilling events in Gale Crater, Mars: Results from morphology, stratigraphy, and mineralogy. *Journal of Geophysical Research: Planets*, 118(12), 2439–2473. https://doi.org/10.1002/2012JE004322
- De Toffoli, B., Mangold, N., Massironi, M., Zanella, A., Pozzobon, R., Le Mouélic, S., et al. (2020). Structural analysis of sulfate vein networks in Gale crater (Mars). *Journal of Structural Geology*, 137, 104083. https://doi.org/10.1016/j.jsg.2020.104083
- Edgar, L., Grotzinger, J., Fedo, C. M., Meyer, M., Rapin, W., Dietrich, W. E., et al. (2024). Wet to dry depositional environments recorded in the clay-sulfate transition region in Gale crater, Mars: Overview and stratigraphic context for Curiosity's Exploration Campaign. In 55th Lunar and Planetary Science Conference (p. 1016). Retrieved from https://hal.science/hal-04442829
- Edgar, L. A., Fedo, C. M., Gupta, S., Banham, S. G., Fraeman, A. A., Grotzinger, J. P., et al. (2020). A lacustrine paleoenvironment recorded at Vera RubinRidge, Gale crater: Overview of the sedimentology and stratigraphy observed by the Mars Science Laboratory Curiosity Rover. Journal of Geophysical Research: Planets, 125(3), e2019JE006307. https://doi.org/10.1029/2019JE006307
- Eng, A. M., Rice, M. S., Farrand, W. H., Johnson, J. R., Jacob, S., Rampe, E. B., et al. (2024). A Mastcam multispectral investigation of rock variability in Gale crater, Mars: Implications for alteration in the clay-sulfate transition of Mount Sharp. *Journal of Geophysical Research: Planets*, 129(2), e2023JE008033. https://doi.org/10.1029/2023JE008033
- Farrand, W. H., Bell, J. F., III, Johnson, J. R., Arvidson, R. E., Crumpler, L. S., Hurowitz, J. A., & Schröder, C. (2008). Rock spectral classes observed by the Spirit Rover's Pancam on the Gusev Crater Plains and in the Columbia Hills. *Journal of Geophysical Research*, 113(E12), E12S38. https://doi.org/10.1029/2008JE003237
- Farrand, W. H., Trussell, A., Eng, A. M., Johnson, J. R., Bell, J. F., Rampe, E. B., et al. (2023). Curiosity Rover Mastcam multispectral measurements of rocks from Marker Band Valley and beyond. In *AGU Fall Meeting Abstracts* (pp. P41E–3219).
- Fedo, C. M., Bryk, A. B., Edgar, L. A., Bennett, K. A., Fox, V. K., Dietrich, W. E., et al. (2022). Geology and stratigraphic correlation of the Murray and Carolyn Shoemaker formations across the Glen Torridon region, Gale crater, Mars. *Journal of Geophysical Research: Planets*, 127(9), e2022JE007408. https://doi.org/10.1029/2022JE007408

TRUSSELL ET AL. 14 of 17

- Fraeman, A. A., Johnson, J. R., Arvidson, R. E., Rice, M. S., Wellington, D. F., Morris, R. V., et al. (2020). Synergistic ground and orbital observations of iron oxides on Mt. Sharp and Vera Rubin ridge. *Journal of Geophysical Research: Planets*, 125(9), e2019JE006294. https://doi.org/10.1029/2019JE006294
- Gasda, P. J., Comellas, J., Essunfeld, A., Das, D., Bryk, A. B., Dehouck, E., et al. (2022). Overview of the morphology and chemistry of diagenetic features in the clay-rich Glen Torridon unit of Gale crater, Mars. *Journal of Geophysical Research: Planets*, 127(12), e2021JE007097. https://doi.org/10.1029/2021JE007097
- Gasda, P. J., Kite, E. S., Thompson, L. M., Mondro, C. A., Dietrich, W. E., Weitz, C. M., et al. (2024). The Amapari Marker Band, Gale Crater, Mars: Metal enrichments and potential mechanisms of formation. In 10th International Conference on Mars 2024. Retrieved from https://hal.science/hal-04650532.3292.
- Gillespie, A. R., Kahle, A. B., & Walker, R. E. (1986). Color enhancement of highly correlated images. I. Decorrelation and HSI contrast stretches. Remote Sensing of Environment, 20(3), 209–235. https://doi.org/10.1016/0034-4257(86)90044-1
- Gómez, F., Rodríguez-Manfredi, J. A., Rodríguez, N., Fernández-Sampedro, M., Caballero-Castrejón, F. J., & Amils, R. (2012). Habitability: Where to look for life? Halophilic habitats: Earth analogs to study Mars habitability. *Planetary and Space Science*, 68(1), 48–55. https://doi.org/10.1016/j.pss.2011.12.021
- Grotzinger, J. P., Crisp, J., Vasavada, A. R., Anderson, R. C., Baker, C. J., Barry, R., et al. (2012). Mars science laboratory Mission and science investigation. Space Science Reviews, 170(1), 5–56. https://doi.org/10.1007/s11214-012-9892-2
- Grotzinger, J. P., Gupta, S., Malin, M. C., Rubin, D. M., Schieber, J., Siebach, K., & Sumner, D. Y. (2015). Deposition, exhumation, and paleoclimate of an ancient lake deposit, Gale crater, Mars. *Science*, 350(6257), aac7575. https://doi.org/10.1126/science.aac7575
- Grotzinger, J. P., Sumner, D. Y., Kah, L. C., Stack, K., Gupta, S., Edgar, L., et al. (2014). A habitable fluvio-lacustrine environment at Yellowknife Bay, Gale crater, Mars. Science, 343(6169), 1242777. https://doi.org/10.1126/science.1242777
- Horgan, B. H. N., Johnson, J. R., Fraeman, A. A., Rice, M. S., Seeger, C., Bell, J. F., III, et al. (2020). Diagenesis of Vera Rubin ridge, Gale crater, Mars, from Mastcam multispectral images. *Journal of Geophysical Research: Planets*, 125(11), e2019JE006322. https://doi.org/10.1029/ 2019JE006322
- Jakosky, B. M. (2021). Atmospheric loss to space and the history of water on Mars. Annual Review of Earth and Planetary Sciences, 49(1), 71–93. https://doi.org/10.1146/annurev-earth-062420-052845
- Johnson, J. R., Bell, J. F., Bender, S., Blaney, D., Cloutis, E., DeFlores, L., et al. (2015). ChemCam passive reflectance spectroscopy of surface materials at the Curiosity landing site, Mars. *Icarus*, 249, 74–92. https://doi.org/10.1016/j.icarus.2014.02.028
- Kronyak, R. E., Kah, L. C., Edgett, K. S., VanBommel, S. J., Thompson, L. M., Wiens, R. C., et al. (2019). Mineral-filled fractures as indicators of multigenerational fluid flow in the Pahrump Hills member of the Murray formation, Gale crater, Mars. Earth and Space Science, 6(2), 238–265. https://doi.org/10.1029/2018EA000482
- Le Mouélic, S., Gasnault, O., Herkenhoff, K. E., Bridges, N. T., Langevin, Y., Mangold, N., et al. (2015). The ChemCam Remote Micro-Imager at Gale crater: Review of the first year of operations on Mars. *Icarus*, 249, 93–107. https://doi.org/10.1016/j.icarus.2014.05.030
- Léveillé, R. J., Bridges, J., Wiens, R. C., Mangold, N., Cousin, A., Lanza, N., et al. (2014). Chemistry of fracture-filling raised ridges in Yellowknife Bay, Gale Crater: Window into past aqueous activity and habitability on Mars. *Journal of Geophysical Research: Planets*, 119(11), 2398–2415. https://doi.org/10.1002/2014JE004620
- L'Haridon, J., Mangold, N., Meslin, P.-Y., Johnson, J. R., Rapin, W., Forni, O., et al. (2018). Chemical variability in mineralized veins observed by ChemCam on the lower slopes of Mount Sharp in Gale crater, Mars. *Icarus*, 311, 69–86. https://doi.org/10.1016/j.icarus.2018.01.028
- Malin, M. C., & Edgett, K. S. (2000). Sedimentary rocks of early Mars. *Science*, 290(5498), 1927–1937. https://doi.org/10.1126/science.290.
- Malin, M. C., Ravine, M. A., Caplinger, M. A., Tony Ghaemi, F., Schaffner, J. A., Maki, J. N., et al. (2017). The Mars Science Laboratory (MSL) Mast cameras and Descent imager: Investigation and instrument descriptions. *Earth and Space Science*, 4(8), 506–539. https://doi.org/10.1002/2016EA000252
- Manelski, H. T., Sheppard, R. Y., Fraeman, A. A., Wiens, R. C., Johnson, J. R., Rampe, E. B., et al. (2023). Compositional variations in sedimentary deposits in Gale Crater as observed by ChemCam passive and active spectra. *Journal of Geophysical Research: Planets*, 128(3), e2022JE007706. https://doi.org/10.1029/2022JE007706
- Maurice, S., Clegg, S. M., Wiens, R. C., Gasnault, O., Rapin, W., Forni, O., et al. (2016). ChemCam activities and discoveries during the nominal mission of the Mars Science Laboratory in Gale crater, Mars. *Journal of Analytical Atomic Spectrometry*, 31(4), 863–889. https://doi.org/10. 1039/C5JA00417A
- Maurice, S., Wiens, R. C., Saccoccio, M., Barraclough, B., Gasnault, O., Forni, O., et al. (2012). The ChemCam instrument suite on the Mars Science Laboratory (MSL) rover: Science objectives and mast unit description. Space Science Reviews, 170(1), 95–166. https://doi.org/10.1007/s11214-012-9912-2
- McLennan, S. M., Anderson, R. B., Bell, J. F., Bridges, J. C., Calef, F., Campbell, J. L., et al. (2014). Elemental geochemistry of sedimentary rocks at Yellowknife Bay, Gale crater, Mars. Science, 343(6169), 1244734. https://doi.org/10.1126/science.1244734
- Meslin, P.-Y., Rapin, W., Forni, O., Cousin, A., Gasnault, O., Loche, M., et al. (2022). Significant halite enrichment in the sulfate-unit of Gale Crater, Mars. In 53rd Lunar and Planetary Science Conference (Vol. 53, p. 2492). Retrieved from https://hal.science/hal-03594170
- Meslin, P. Y., Rapin, W., Forni, O., Cousin, A., Gasnault, O., Loche, M., et al. (2024). Overview of halite detections by chemcam in Gale crater, Mars. In 10th International Conference on Mars 2024. LPI Contribution No. 3007.
- Meyer, M. J., Milliken, R. E., Stack, K. M., Edgar, L. A., Rampe, E. B., Turner, M. L., et al. (2024). Geological context and significance of the clay-sulfate transition region in Mount Sharp, Gale crater, Mars: An integrated assessment based on orbiter and rover data. *GSA Bulletin*, 137(1–2), 82–115. https://doi.org/10.1130/B37355.1
- Milliken, R. E., Grotzinger, J. P., & Thomson, B. J. (2010). Paleoclimate of Mars as captured by the stratigraphic record in Gale Crater. Geophysical Research Letters, 37(4), L04201. https://doi.org/10.1029/2009GL041870
- Mondro, C. A., Fedo, C. M., Grotzinger, J. P., Lamb, M. P., Gupta, S., Dietrich, W. E., et al. (2025). Wave ripples formed in ancient, ice-free lakes in Gale crater, Mars. *Science Advances*, 11(3), eadr0010. https://doi.org/10.1126/sciadv.adr0010
- Nachon, M., Clegg, S. M., Mangold, N., Schröder, S., Kah, L. C., Dromart, G., et al. (2014). Calcium sulfate veins characterized by ChemCam/Curiosity at Gale crater, Mars. *Journal of Geophysical Research: Planets*, 119(9), 1991–2016. https://doi.org/10.1002/2013JE004588
- Nachon, M., Mangold, N., Forni, O., Kah, L. C., Cousin, A., Wiens, R. C., et al. (2017). Chemistry of diagenetic features analyzed by ChemCam at Pahrump Hills, Gale crater, Mars. *Icarus*, 281, 121–136. https://doi.org/10.1016/j.icarus.2016.08.026
- O'Connell-Cooper, C. D., Spray, J. G., Gellert, R., Thompson, L. M., Berger, J., Boyd, N. I., et al. (2025). Salty Mars—Na enrichments associated with Cl, S, Mg, Ca in the layered sulfate unit, Gale Crater, Mars: APXS identification and implications. In 56th Lunar and Planetary Science Conference

TRUSSELL ET AL. 15 of 17



- 10.1029/2025JE009244
- O'Connell-Cooper, C. D., Thompson, L. M., Spray, J. G., Gellert, R., McCraig, M. A., Boyd, N. I., et al. (2024). APXS geochemistry of the Chenapau member, Gale crater, Mars and a comparison of lithologies above and below the Amapari Marker Band. In 55th lunar and planetary science conference (Vol. 3040).2382.
- Paar, G., Ortner, T., Tate, C., Deen, R. G., Abercrombie, P., Vona, M., et al. (2023). Three-dimensional data preparation and immersive mission-spanning visualization and analysis of Mars 2020 Mastcam-Z stereo image sequences. *Earth and Space Science*, 10(3), e2022EA002532. https://doi.org/10.1029/2022EA002532
- Planetary Data System Cartography and Imaging Sciences Node. (2025). Planetary Data System Cartography and Imaging Sciences Node [Dataset]. *Planetary Data System*. Retrieved from https://pds-imaging.jpl.nasa.gov/volumes/msl.html
- Planetary Data System (PDS) Geosciences Node. (2025). Planetary Data System (PDS) Geosciences Node [Dataset]. *Planetary Data System*. Retrieved from https://pds-geosciences.wustl.edu/missions/msl/chemcam.htm
- Rampe, E. B., Bristow, T. F., Blake, D. F., Vaniman, D. T., Chipera, S. J., Downs, R. T., et al. (2022). Mineralogical trends over the clay-sulfate transition in Gale Crater from the Mars Science Laboratory CheMin Instrument. In 53rd Lunar and Planetary Science Conference, The Woodlands, TX. Retrieved from https://ntrs.nasa.gov/citations/20210026241
- Rampe, E. B., Ming, D. W., Blake, D. F., Bristow, T. F., Chipera, S. J., Grotzinger, J. P., et al. (2017). Mineralogy of an ancient lacustrine mudstone succession from the Murray formation, Gale crater, Mars. Earth and Planetary Science Letters, 471, 172–185. https://doi.org/10. 1016/j.epsl.2017.04.021
- Rapin, W., Dromart, G., Clark, B. C., Schieber, J., Kite, E. S., Kah, L. C., et al. (2023). Sustained wet-dry cycling on early Mars. *Nature*, 620(7973), 299–302. https://doi.org/10.1038/s41586-023-06220-3
- Rapin, W., Dromart, G., Rubin, D., Deit, L. L., Mangold, N., Edgar, L. A., et al. (2021). Alternating wet and dry depositional environments recorded in the stratigraphy of Mount Sharp at Gale crater, Mars. *Geology*, 49(7), 842–846. https://doi.org/10.1130/G48519.1
- Rapin, W., Ehlmann, B. L., Dromart, G., Schieber, J., Thomas, N. H., Fischer, W. W., et al. (2019). An interval of high salinity in ancient Gale crater lake on Mars. *Nature Geoscience*, 12(11), 889–895. https://doi.org/10.1038/s41561-019-0458-8
- Rapin, W., Meslin, P.-Y., Maurice, S., Vaniman, D., Nachon, M., Mangold, N., et al. (2016). Hydration state of calcium sulfates in Gale crater, Mars: Identification of bassanite veins. Earth and Planetary Science Letters, 452, 197–205. https://doi.org/10.1016/j.epsl.2016.07.045
- Mars: Identification of bassanite veins. Earth and Planetary Science Letters, 452, 197–205. https://doi.org/10.1016/j.epsl.2016.07.045
  Rice, M. S., Bell, J. F., Cloutis, E. A., Wang, A., Ruff, S. W., Craig, M. A., et al. (2010). Silica-rich deposits and hydrated minerals at Gusev
- Crater, Mars: Vis-NIR spectral characterization and regional mapping. *Icarus*, 205(2), 375–395. https://doi.org/10.1016/j.icarus.2009.03.035 Rice, M. S., Seeger, C., Bell, J., Calef, F., St. Clair, M., Eng, A., et al. (2022). Spectral diversity of rocks and soils in Mastcam observations along the Curiosity rover's traverse in Gale crater, Mars. *Journal of Geophysical Research: Planets*, 127(8), e2021JE007134. https://doi.org/10.1029/2021JE007134
- Roberts, A. L., Gupta, S., Banham, S. G., Cowart, A., Edgar, L. A., Rapin, W., et al. (2025). Paleo-scours within the layered sulfate-bearing unit at Gale Crater, Mars: Evidence for intense wind erosion. *Journal of Geophysical Research: Planets*, 130(5), e2024JE008680. https://doi.org/10.1029/2024JE008680
- Roberts, A. L., Gupta, S., Cowart, A., Edgar, L., Dietrich, W. E., Rapin, W., et al. (2024). Depositional processes and environments of the layered sulfate-bearing unit, Gale crater, Mars. In 10th International Conference on Mars 2024 (p. 3515). Retrieved from https://hal.science/hal-
- Roberts, A. L., Gupta, S., Dietrich, W. E., Edgar, L. A., Rapin, W., Banham, S. G., et al. (2023). What depositional processes and paleoenvironments formed the layered sulfate unit in Gale crater, Mars? Insights from Marker Band valley. In 54th Lunar and Planetary Science Conference (Vol. 54, p. 2945). Retrieved from https://hal.science/hal-04052600
- Rodriguez, J. A. P., Kargel, J. S., Baker, V. R., Gulick, V. C., Berman, D. C., Fairén, A. G., et al. (2015). Martian outflow channels: How did their source aquifers form and why did they drain so rapidly? *Scientific Reports*, 5(1), 13404. https://doi.org/10.1038/srep13404
- Scheller, E. L., Ehlmann, B. L., Hu, R., Adams, D. J., & Yung, Y. L. (2021). Long-term drying of Mars by sequestration of ocean-scale volumes of water in the crust. *Science*, 372(6537), 56–62. https://doi.org/10.1126/science.abc7717
- Schwenzer, S. P., Bridges, J. C., Wiens, R. C., Conrad, P. G., Kelley, S. P., Leveille, R., et al. (2016). Fluids during diagenesis and sulfate vein formation in sediments at Gale crater, Mars. *Meteoritics & Planetary Science*, 51(11), 2175–2202. https://doi.org/10.1111/maps.12668
- Seeger, C. H., & Grotzinger, J. P. (2024). Diagenesis of the clay-sulfate stratigraphic transition, Mount Sharp Group, Gale Crater, Mars. Journal of Geophysical Research: Planets, 129(12), e2024JE008531. https://doi.org/10.1029/2024JE008531
- Stack, K. M., Grotzinger, J. P., Kah, L. C., Schmidt, M. E., Mangold, N., Edgett, K. S., et al. (2014). Diagenetic origin of nodules in the Sheepbed member, Yellowknife Bay formation, Gale crater, Mars. *Journal of Geophysical Research: Planets*, 119(7), 1637–1664. https://doi.org/10.1002/2014JE004617
- Stack, K. M., Grotzinger, J. P., Lamb, M. P., Gupta, S., Rubin, D. M., Kah, L. C., et al. (2019). Evidence for plunging river plume deposits in the Pahrump Hills member of the Murray formation, Gale crater, Mars. Sedimentology, 66(5), 1768–1802. https://doi.org/10.1111/sed.12558
- Stein, N., Grotzinger, J. P., Schieber, J., Mangold, N., Hallet, B., Newsom, H., et al. (2018). Desiccation cracks provide evidence of lake drying on Mars, Sutton Island member, Murray formation, Gale Crater. *Geology*, 46(6), 515–518. https://doi.org/10.1130/G40005.1
- Tanaka, K. L., Skinner, J. A., Dohm, J. M., Iii, R. P. I., Kolb, E. J., Fortezzo, C. M., et al. (2014). Geologic map of Mars. In *Scientific Investigations Map* (Vol. 3292). U.S. Geological Survey. https://doi.org/10.3133/sim3292
- Thomas, N. H., Ehlmann, B. L., Anderson, D. E., Clegg, S. M., Forni, O., Schröder, S., et al. (2018). Characterization of hydrogen in basaltic materials with laser-induced breakdown spectroscopy (LIBS) for application to MSL ChemCam data. *Journal of Geophysical Research: Planets*, 123(8), 1996–2021. https://doi.org/10.1029/2017JE005467
- Thomas, N. H., Ehlmann, B. L., Meslin, P.-Y., Rapin, W., Anderson, D. E., Rivera-Hernández, F., et al. (2019). Mars Science Laboratory observations of chloride salts in Gale crater, Mars. Geophysical Research Letters, 46(19), 10754–10763. https://doi.org/10.1029/2019GL082764
- Thomson, B. J., Bridges, N. T., Milliken, R., Baldridge, A., Hook, S. J., Crowley, J. K., et al. (2011). Constraints on the origin and evolution of the layered mound in Gale Crater, Mars using Mars Reconnaissance Orbiter data. *Icarus*, 214(2), 413–432. https://doi.org/10.1016/j.icarus.2011.05.002
- Tosca, N. J., & McLennan, S. M. (2006). Chemical divides and evaporite assemblages on Mars. Earth and Planetary Science Letters, 241(1), 21–31. https://doi.org/10.1016/j.epsl.2005.10.021
- Traxler, C., Ortner, T., Hesina, G., Barnes, R., Gupta, S., Paar, G., et al. (2022). The PRoViDE Framework: Accurate 3D geological models for virtual exploration of the Martian surface from rover and orbital imagery. In 3D digital geological models (pp. 33–55). John Wiley & Sons, Ltd. https://doi.org/10.1002/9781119313922.ch3
- Treiman, A. H., Lanza, N. L., VanBommel, S., Berger, J., Wiens, R., Bristow, T., et al. (2023). Manganese-iron phosphate nodules at the Groken site, Gale crater, Mars. *Minerals*, 13(9), 9. https://doi.org/10.3390/min13091122
- Trussell, A. (2025). Supplementary data for dark-toned halite-enriched veins above the Marker Band record a drying environment in Gale crater [Dataset]. Zenodo. https://doi.org/10.5281/zenodo.15611155

TRUSSELL ET AL. 16 of 17

- Tutolo, B. M., Hausrath, E. M., Kite, E. S., Rampe, E. B., Bristow, T. F., Downs, R. T., et al. (2025). Carbonates identified by the Curiosity rover indicate a carbon cycle operated on ancient Mars. Science, 388(6744), 292–297. https://doi.org/10.1126/science.ado9966
- VanBommel, S. J., Berger, J. A., Gellert, R., O'Connell-Cooper, C. D., McCraig, M. A., Thompson, L. M., et al. (2023). Elemental composition of manganese- and phosphorus-rich nodules in the Knockfarril Hill member, Gale crater, Mars. *Icarus*, 392, 115372. https://doi.org/10.1016/j. icarus.2022.115372
- Vasavada, A. R. (2022). Mission overview and scientific contributions from the Mars Science Laboratory Curiosity Rover after eight years of surface operations. Space Science Reviews, 218(3), 3. https://doi.org/10.1007/s11214-022-00882-7
- Watkins, J. A., Grotzinger, J. P., Stein, N. T., Banham, S. G., Gupta, S., Rubin, D. M., et al. (2022). Burial and exhumation of sedimentary rocks revealed by the base Stimson erosional unconformity, Gale crater, Mars. *Journal of Geophysical Research: Planets*, 127(7), e2022JE007293. https://doi.org/10.1029/2022JE007293
- Wellington, D. F., Bell, J. F., Johnson, J. R., Kinch, K. M., Rice, M. S., Godber, A., et al. (2017). Visible to near-infrared MSL/Mastcam multispectral imaging: Initial results from select high-interest science targets within Gale Crater, Mars. *American Mineralogist*, 102(6), 1202–1217. https://doi.org/10.2138/am-2017-5760CCBY
- Wiens, R. C., Maurice, S., & MSL Science Team. (2015). ChemCam: Chemostratigraphy by the first Mars microprobe. *Elements*, 11(1), 33–38. https://doi.org/10.2113/gselements.11.1.33
- Wiens, R. C., Maurice, S., Barraclough, B., Saccoccio, M., Barkley, W. C., Bell, J. F., et al. (2012). The ChemCam instrument suite on the Mars Science Laboratory (MSL) Rover: Body unit and combined system tests. *Space Science Reviews*, 170(1), 167–227. https://doi.org/10.1007/s11214-012-9902-4
- Wiens, R. C., Maurice, S., Lasue, J., Forni, O., Anderson, R. B., Clegg, S., et al. (2013). Pre-flight calibration and initial data processing for the ChemCam laser-induced breakdown spectroscopy instrument on the Mars Science Laboratory rover. *Spectroschimica Acta Part B: Atomic Spectroscopy*, 82, 1–27. https://doi.org/10.1016/j.sab.2013.02.003
- Wiens, R. C., Rubin, D. M., Goetz, W., Fairén, A. G., Schwenzer, S. P., Johnson, J. R., et al. (2017). Centimeter to decimeter hollow concretions and voids in Gale Crater sediments, Mars. *Icarus*, 289, 144–156. https://doi.org/10.1016/j.icarus.2017.02.003

TRUSSELL ET AL. 17 of 17